Morphology-induced shape selectivity in zeolite catalysis

CrossMark

Shewangizaw Teketel [a], Lars F. Lundegaard [b], Wegard Skistad [a], Sachin M. Chavan [a], Unni Olsbye [a], Karl Petter Lillerud [a], Pablo Beato [b],*, Stian Svelle [a],*

[a] inGAP Center of Research Based Innovation, Department of Chemistry, University of Oslo, P.O. Box 1033, Blindern, N-0315 Oslo, Norway
[b] Haldor Topsøe A/S, Nymøllevej 55, 2800 Kgs. Lyngby, Denmark

ABSTRACT

Zeolites are crystalline aluminosilicates that are widely used as shape-selective catalysts in the refinery and petrochemical industries. By synthesizing a series of structurally related zeolite catalyst and applying them in the industrially relevant conversion of methanol to hydrocarbons, new and extended understanding of the concept of shape selectivity has been reached. We have analyzed the relationship between particle morphology and pore system for catalysts having both small- and medium-sized pores using microscopy and diffraction, as well as performing extensive standard characterization. Two instances of preferential exposure of certain crystal facets, favoring access to one pore system over the other, have been found. Zeolites ZSM-57 (MFS) and SUZ-4 (SZR) both have both 8- and 10-ring channels. MFS prefers a plate-like or nanosheet-type morphology, where the 10-ring channels are perpendicular to the plates/sheets. This leads to favorable diffusion properties and a pronounced deactivation resistance. For SZR, needle-like crystals with high aspect ratio are preferred. In this instance, the sides of the needles are covered by the 8-ring pore openings, whereas the 10-ring pore openings are only exposed at the ends of the needles. This leads to unexpected product selectivity, as the material behaves essentially as an 8-ring catalyst. We argue that it should be possible to tune the shape selectivity of zeolite catalysts having pore systems of different dimensions by controlling the crystal morphology.

© 2015 Elsevier Inc. All rights reserved.

1. Introduction

The defining characteristic of microporous zeolite catalysts is that they possess strong Brønsted acid sites, which are dispersed within regular pores of molecular dimensions. The confined space around the active sites and the restricted access to and exit from the internal surface gives rise to the widespread use of zeolites as shape-selective catalysts in the refinery and petrochemical industries. The shape-selective behavior of zeolites is frequently discussed based on simple mass transport limitations or transition state control of reactions [1]. This provides an adequate rationalization of the well-known reactant shape selectivity, product shape selectivity, and transition state selectivity, which is sometimes expanded to include steric manipulation also of reaction intermediates [2,3]. However, several other and more diffuse aspects of shape selectivity are occasionally encountered, such as molecular traffic control [4] and inverse shape selectivity [5], as well as surface effects such as the "nest" effect [6], pore mouth catalysis [7,8], and key–lock shape selectivity [9,10]. Thus, shape selectivity is a complex phenomenon, and the parameters that induce shape selectivity in zeolite catalysis are not always fully understood and/or a priori predictable.

One process that uses zeolites as shape-selective catalysts is the conversion of methanol to hydrocarbons (MTH), which is a generic term for a group of industrial processes [11]. The MTH product may be an aromatic and paraffin-rich high octane gasoline mixture (MTG); light alkenes (methanol to olefins – MTO); or mainly propene with some gasoline by-product (methanol to propene – MTP) [12]. Clearly, the product distribution of the MTH reaction depends on reaction conditions, but it is to a great extent predictable based on product shape selectivity arguments. That is, small-pore zeolites will give mainly light olefins, while medium- and large-pore zeolites give heavier hydrocarbons. However, for catalysts with more complex pore systems, consisting of combinations of pores (small and medium or medium and large, etc.), and/or pore extensions (side pockets), the shape selectivity is less predictable. For example, studies of the MTH reaction over MWW (MCM-22) and EUO (EU-1) zeolites have reported unexpected product distribution, due to contributions from side pockets located at the exterior surface of the crystals [13,14].

---

* Corresponding authors.
  E-mail addresses: pabb@topsoe.dk (P. Beato), stian.svelle@kjemi.uio.no (S. Svelle).

About 200 distinct framework topologies are described in the database of the International Zeolite Association, and the list increases by 5–10 members every year [15]. Efforts to match novel and existing zeolite structures with new or improved applications require both the optimum tools and concise concepts to identify zeolite catalysts suitable for the desired applications in a predictable manner. Smit and Maesen highlighted that computer simulation can provide valuable and detailed mechanistic insights into the nucleation and crystal growth of zeolites, which eventually might lead to a rational zeolite choice from the continuously growing database [16,17]. In this contribution, we highlight how particle morphology may influence the access to the zeolite internal surface and thus become a tunable parameter giving rise to shape selectivity in zeolite catalysis. The effects of preferential exposure of certain crystal facets are well documented within other areas of catalysis, such as nanoparticle-based catalysis [18–20], but appear to have received less attention or to have been addressed from a somewhat different perspective within zeolite catalysis.

Several reviews cover the creation of secondary mesopores or hierarchical structures and catalytic application of such zeolite materials [21–30]. Most of these report improved deactivation resistance and access to active sites. The importance of extra-large-pore zeolites as catalysts and their ability to process bulky molecules have been demonstrated most clearly by Corma and co-workers [31,32]. Particle size is also an important parameter for zeolite applications, which may influence both catalyst lifetime and selectivities [33–36]. The roles of intergrowths within zeolite crystals and the effects of these on diffusion have been highlighted [37,38]. Layered two-dimensional zeolite materials typically show high accessibility to and reactivity of the active sites [39,40]. Of particular impact are the recent efforts of Ryoo and co-workers [41,42] on unit cell thick ZSM-5 nanosheets, which also address the effects of morphology on shape selectivity. It thus appears that most of the literature that concerns the effect of zeolite particle morphology and catalytic performance, some of which is cited above, is essentially based on the alterations of the access to or from the active sites by tuning *diffusion lengths*, either by creating mesopores, adjusting the particle size and shape, or by synthesizing layered materials by various methods.

In this work, the shape selectivity of nine zeolite catalysts comprising different combinations of 8- and 10-ring pores, namely EUO (EU-1), FER (Ferrierite), CHA (SAPO-34), SZR (SUZ-4), (MFI) (ZSM-5), TON (ZSM-22), MTT (ZSM-23), *MRE (ZSM-48), and MFS (ZSM-57) has been investigated in the MTH process. To the best of our knowledge, MFS and SZR have not previously been investigated as catalysts in the MTH reaction. One report concerning methanol dehydration into dimethyl ether exists for SZR [43]. During these systematic studies of the effects of zeolite topology on catalyst performance in the MTH reaction [13,44], we have encountered two separate instances where the catalyst performance is determined predominantly by particle morphology, and in particular, how the framework topology is structurally related to the morphology. These observations were made for the SZR (SUZ-4) and MFS (ZSM-57) catalysts. For SZR, unexpected and remarkable results were obtained, and it is demonstrated that the product shape selectivity is determined by the *preferential exposure of certain crystal facets* that effectively forces the products to leave the crystals via the narrow 8-rings and not the 10-rings, which would otherwise be preferred. For MFS, a profound deactivation resistance is observed, which we attribute to short diffusion pathways in line with previous reports [42]. Finally, analysis of the morphology using transmission electron microscopy (TEM) crystallographic and imaging methods, bulk X-ray diffraction analysis, and crystal growth simulation revealed that for these two catalysts (SZR and MFS), the data inferred from the ideal crystal structure alone do not provide a sufficient background for a discussion of their shape-selective properties.

Professor Jean-Pierre Gilson graduated with a doctorate in science from the University of Namur in 1982 in collaboration with Eric G. Derouane and with the support of Haldor Topsøe A/S. Throughout his research career, he has worked extensively with shape selectivity and zeolite catalysts. We cannot be exhaustive here, but we would like to mention that he has reviewed the basis of zeolites as shape-selective catalysts together with Guisnet [45], and he has reviewed the use of zeolites in the petroleum and petrochemical industry with Vermeiren [46]. He has studied a number of acid-catalyzed reactions, including the conversion of methanol to hydrocarbons already in 1979 [47], and (as director of the catalysis and spectrochemistry lab in Caen) he has applied infrared spectroscopy extensively in his zeolite research. More recently, he has studied also the morphology of zeolite catalysts, with particular emphasis on nanosized [48] and hierarchical materials [49,50]. Thus, it is clear that Jean-Pierre has contributed significantly to our understanding of virtually all areas encountered in this contribution, which we are particularly pleased to dedicate to him on the occasion of his 60th birthday!

2. Catalysts

Nine different catalysts are employed in this work; one silicoaluminophosphate zeotype and eight aluminosilicate zeolites. The topologies (see Table 1 and Fig. 1) of these catalysts contain many of the same structural elements. Based on the dimensionality of the pores in the idealized framework, the nine topologies fall into three categories: one-dimensional (TON, MTT, *MRE, EUO), two-dimensional (FER, MFS), and three-dimensional (CHA, SZR, MFI). The structure of each of the materials is discussed in the Supplementary Material.

3. Experimental

3.1. Catalyst preparation

Except for Ferrierite, ZSM-5, and ZSM-23, the materials in this work were synthesized in-house under hydrothermal conditions. Details on the synthesis procedures are presented in the Supplementary Material. The syntheses are based on procedures detailed in Refs. [13,43,51–53]. The synthesized ZSM-22, EU-1, ZSM-48, SUZ-4, and ZSM-57 catalysts were ion-exchanged and calcined after the removal of the structure-directing agent. The calcined material was ion-exchanged three times for 2 h with 1 M NH_4NO_3 at 70 °C. The ion-exchanged catalysts were calcined

Table 1
Key structural data for the zeolite catalyst studied, from [15].

Topology (material)	Channel dimensionality	10-Ring	8-Ring(s)	d_{max}[a] (Å)
EUO (EU-1)[b]	1D	4.1 × 5.4 Å	None	7.0
FER (Ferrierite)	2D	4.2 × 5.4 Å	3.5 × 4.8 Å	6.3
CHA (SAPO-34)	3D	None	3.8 × 3.8 Å	7.4
SZR (SUZ-4)	3D	4.1 × 5.2 Å	3.0 × 4.8 Å	6.3
			3.2 × 4.8 Å	
MFI (ZSM-5)	3D	5.3 × 5.5 Å	None	6.4
		5.4 × 5.6 Å		
TON (ZSM-22)	1D	4.6 × 5.7 Å	None	5.7
MTT (ZSM-23)	1D	4.5 × 5.2 Å	None	6.2
*MRE (ZSM-48)	1D	5.3 × 5.6 Å	None	6.4
MFS (ZSM-57)	2D	5.1 × 5.4 Å	3.3 × 4.8 Å	6.8

[a] Maximum diameter of a sphere that can be included inside the largest cavity/intersection.
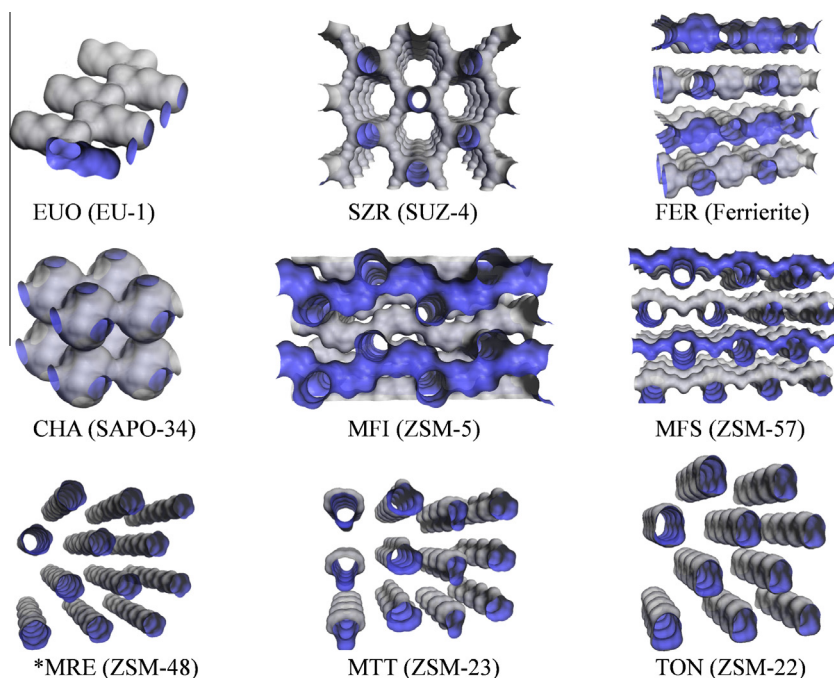
[b] Has large 12-ring side pockets.

Fig. 1. Illustration of the pore systems of the materials included in this work. The blue color represents the interior of the pores. (For interpretation of the references to color in this figure legend, the reader is referred to the web version of this article.)

at 550 °C for 2 h in static air followed by 1 h in a flow of pure oxygen to desorb ammonia.

3.2. Catalyst characterization

Several techniques were employed to characterize the catalysts under study. As we consider the results found for the SZR (SUZ-4) and MFS (ZSM-57) catalysts to be of particular interest, these materials were subjected to a more thorough characterization.

Powder XRD data were collected on a Philips X'Pert (Cu Kα) diffractometer. The crystallinity and purity of the material were confirmed by full-profile LeBail analysis.

The size, morphology, and the Si/Al ratio of the catalyst particles were determined with scanning electron microscopy. Micrographs were recorded on either FEI Quanta 200 FEG-ESEM equipped with an Everhart–Thornley detector and an EDAX EDS detector or Phillips XL30 ESEM™FEG Environmental Scanning Electron Microscope.

TEM imaging and selected area electron diffraction (SAED) were performed as described elsewhere [54]. Gold was used as internal diffraction standard to obtain exact lattice spacings.

The BET surface area and pore volume were determined by nitrogen physisorption measurements at liquid nitrogen temperature (in a range of relative pressure 0–0.99 p/p_0) on a Belsorp-mini II instrument. The sample was outgassed under vacuum for 5 h, 1 h at 80 °C, and 4 h at 300 °C before the measurement.

Temperature-programmed desorption of *n*-propylamine was performed as described by Gorte et al. [55,56] to quantify the density of acid sites for SZR and MFS. 10–20 mg of catalyst was spread in an 11-mm glass reactor forming a thin bed. The catalyst was pretreated in a flow of oxygen at 550 °C and cooled down to 150 °C. A stream of N_2 was then directed to a saturator with *n*-propylamine at room temperature and fed to the reactor for about 20 min to adsorb *n*-propylamine. Afterward, the catalyst was flushed with N_2 at 150 °C to desorb the excess of the amine. The temperature was subsequently ramped at 20 °C/min up to 550 °C, and the amount of the expected products, propene (and ammonia),

was quantified by using an online Pfeiffer Omnistar quadrupole mass spectrometer. Each sample was measured twice, and no significant variation was seen between the measurements.

FT-IR measurements with CO as probe molecule were performed on a Bruker Vertex 80 instrument with MCT detector. A thin sample wafer was supported in a gold envelope enclosed in an in-house-constructed quartz transmission cell with KBr windows. The sample was pretreated at 150 °C for 1 h, at 300 °C for 1 h, and at 450 °C for 1 h under vacuum. CO was introduced and the sample was cooled to liquid nitrogen temperature. Subsequently, spectra were recorded during desorption by evacuation.

FT-IR measurements with pyridine as probe molecule were performed on a Bruker Vertex 70 instrument with DTGS detector and a Harrick high-temperature transmission cell with KBr windows. Sample wafers were activated by heating to 450 °C in a flow of synthetic air. Subsequently, the sample was cooled to 150 °C, and pyridine was introduced by switching to a nitrogen stream (40 mL min^{-1}) saturated with pyridine at 20 °C. The sample was considered saturated when no further spectral changes occurred. Finally, the sample temperature was increased with 50 °C intervals to 400 °C. Several spectra were recorded at each temperature. The concentration of acid sites was determined using the extinction coefficients reported by Selli and Forni [57]. The spectra recorded at 200 °C were used for the quantitative analysis (rather than the more common 150 °C) due to the use of a flow cell rather than vacuum equipment.

Uptake measurements were performed in a Stanton Redcroft TGA instrument, where the sample is placed in a crucible. Prior to the uptake, the catalysts were dried by heating to 550 °C in flowing helium. After cooling to 100 °C, the helium stream was saturated with methanol or 2,2-dimethylbutane at 0 °C and the increase in mass was observed for 200 min. Clearly, such a basic setup with its ill-defined gas flow pattern does not allow the determination of actual diffusion coefficients, but the measurements using 2,2-dimethylbutane nevertheless provide some indication on the ease with which a relatively bulky molecule may gain access to the interior of the zeolite crystals.

The crystal shape of SZR and FER was simulated using the Bravais–Friedel Donnay–Harker (BFDH) method as implemented in Materials Studio 7.0. The BFDH method allows the estimation of the morphology from the crystal symmetry and the lattice parameters without taking into account the chemical nature and packing of the atoms or molecules that form the crystal. The purpose of the simulations was to illustrate how the crystal structure may be embedded into crystals of the observed morphology.

3.3. Catalytic tests

The catalytic experiments were performed using fixed-bed glass reactors (i.d. 10 mm) and 50 mg catalyst. The protonated catalyst was pressed, gently crushed, and sieved to particle sizes between 250 and 420 μm. Before each test, the reactor was heated to 550 °C under a flow of helium. The catalysts were calcined in situ at this temperature with a flow of pure oxygen for 1 h. The in situ calcination is performed to remove species adsorbed during catalyst handling and storage and is important for the reproducibility of the results. The reaction products were analyzed by an online gas chromatograph connected to the outlet of the reactor via a heated transfer line. An Agilent 6890 A GC with FID using a Supelco SPB-5 capillary column (60 m, 0.530 mm i.d., stationary phase thickness 3 μm) was used for the analysis. The temperature was programmed between 45 and 260 °C with a heating rate of 25 °C min^{-1} (hold time = 5 min at 45 °C and 16 min at the final temperature).

4. Results

4.1. General catalyst characterization

Table 2 summarizes the main characteristics of the catalysts. The composition of the materials was determined using EDS. The frequency shift observed during CO adsorption (Fig. S.1 of the Supplementary Material) is a measure of the acid strength of Brønsted acid sites in zeolites and zeotype materials [58,59]. The values presented for the materials in this work are in the range expected from zeolites, which are indistinguishable in acid strength as measured by this approach. SAPO materials are weaker in acid strength than zeolites [60–62], as a result the frequency shift observed on SAPO-34 is the smallest in this work. The BET surface areas agree well with previously reported values; however, the surface area for the commercial MTT catalyst is somewhat low [13,51,63–66]. The particle shapes and sizes presented for the materials are observed from the SEM images in Fig. S.2.

Table 2
Main characteristics of the investigated catalysts.

Topology (material)	Si/Al ratio[a]	Δv((OH) (cm^{-1}) upon CO adsorption	BET area (m^2 g^{-1})	Particle shape	Particle size (μm)
EUO (EU-1)	30	310	420	Rods	<1
FER (Ferrierite)	11	312	352	Irregular plates	1–10
CHA (SAPO-34)	11[b]	274	NA	Cubes	1–2
SZR (SUZ-4)	8	301	346	Needles	2–5
MFI (ZSM-5)	50	302	430	Round/ agglomerates	1–2
TON (ZSM-22)	30	320	207	Needles	2–3
MTT (ZSM-23)	33	330	115	Rods/ needles	<1
*MRE (ZSM-48)	52	NA[c]	275	Rods	1–2
MFS (ZSM-57)	30	326	421	Plates	~1

[a] From EDS.
[b] (Al + P)/Si.
[c] Not available.

As seen from Table 2, the catalysts display different particle shapes and sizes as well as different surface areas and acid site densities. Clearly, it would have been beneficial to investigate a set of samples with more comparable physicochemical properties. However, this would require a formidable synthesis effort, beyond the substantial effort already made. Moreover, it is doubtful whether this would even be feasible, as some materials crystallize within fairly narrow composition ranges (e.g. no reports exist for the preparation of SZR with Si/Al higher than 9) and most of the materials with 1D pore systems show a strong preference for elongated crystals. Thus, in the following, emphasis will be placed primarily on the major observations made and conclusion which may be safely ascribed to the influence of catalyst morphology.

4.2. Extended characterization of SZR and MFS

Fig. 2 shows powder XRD data of SZR (panel A) and MFS (panel B). The crystallinity and purity of the materials are confirmed by full-profile LeBail analysis. The difference curve reveals anisotropy in the peak broadening, which is related to the anisotropic morphology of the crystallites. In the case of SZR, the observed peaks with indices ($h k 0$) are broader relative to the model peaks, for which isotropic particle shape has been assumed. In contrast, observed ($0 0 l$) peaks are sharper compared with model peaks. Notice how the difference curve for broad peaks is pointing down while it is pointing up for sharp peaks. These observations are consistent with a c-axis parallel to the needle morphology as observed using electron microscopy (Figs. S.2 and 5). In the case of MFS, the observed peaks of the type ($0 k l$) are relatively sharp, while observed peaks with a nonzero h index are relatively broad. This is consistent with the a-axis being perpendicular to the plate morphology observed using electron microscopy (Figs. S.2 and 6).

The acidity of SZR and MFS was characterized using TPD of n-propylamine. By monitoring the evolution of propene from decomposition of n-propylamine during heating, the density of acid sites was determined to be 0.46 mmol g^{-1} for MFS and 0.63 mmol g^{-1} for SZR. Assuming that one acid site corresponds to one Al, this gives Si/Al ratios of 36 for MFS and 26 for SZR. Thus, for MFS, this measurement agrees well with the sample composition from EDS (Si/Al = 30 from EDS, Table 2). For SZR, however, a significant discrepancy is observed (Si/Al = 8 from EDS, Table 2). This could suggest that some of the acid sites in SZR are inaccessible, that some of the acid sites are located too closely to facilitate accommodation of probe molecules on every site, or that some of the sites are too weakly acidic to protonate the amine. It has previously been reported that TPD of n-propylamine underestimates the acid site density for high Al materials [67]. It is likely that some of the Al present in the sample does not give rise to acidity. This is linked to non-exchangeable potassium cations present in cages in the structure [68]. Lawton et al. [68] have reported that only about 50% of the potassium cations were exchangeable (sample Si/Al = 6), whereas Zholobenko et al. [69] were able to exchange 75% (sample Si/Al = 6).

FT-IR characterization of SZR and MFS was performed using both pyridine and CO as probe molecules. Turning first to the spectra of the dehydrated catalysts (Figs. 3 and 4; also shown in Fig. S.3 for clarity), several bands are seen in the hydroxyl stretching region, which may be assigned as follows [70]. Sharp bands seen at 3750/3749 cm^{-1} correspond to isolated/terminal silanols, whereas the shoulders extending to lower wavenumbers are signatures of silanol groups involved in hydrogen bonding. Bridging hydroxyls (Brønsted sites) are seen at 3613 cm^{-1}. For MFS, a small but distinct feature is seen at 3662 cm^{-1}, which may be attributed to hydroxyl groups attached to partial extra framework Al species. For SZR, a broad band is seen centered at 3651 cm^{-1}. Definitive assignment is not (yet) straightforward. Plausible explanations
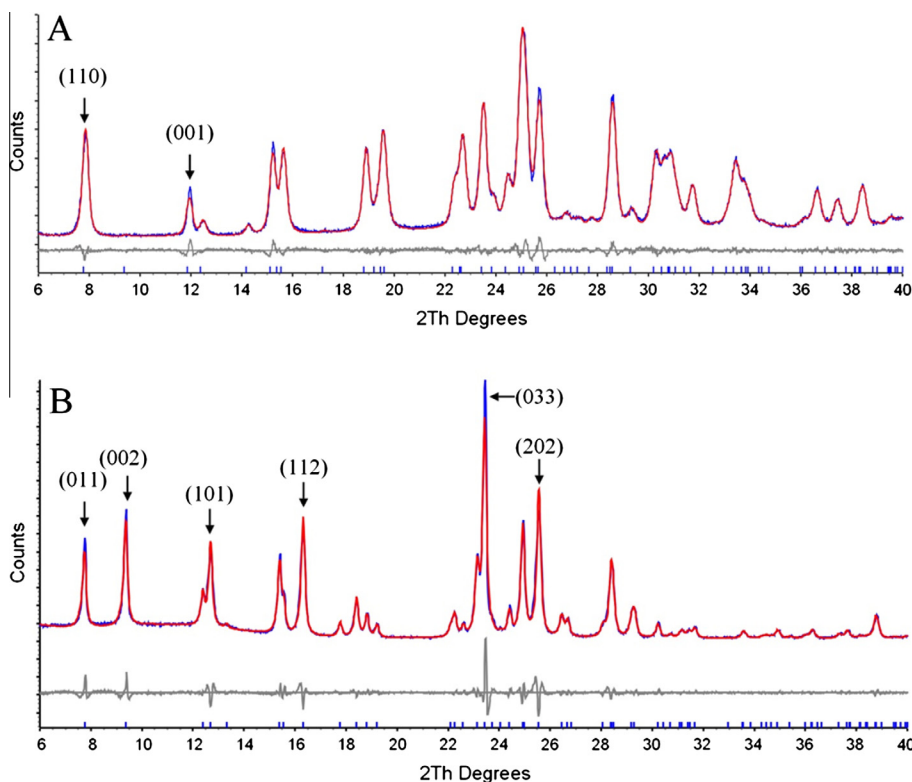
Fig. 2. Full-profile powder XRD data analysis. (A) LeBail analysis of the SZR data. (B) LeBail analysis of the MFS data. The blue and the red curves are observed and model data, respectively. The gray curve is the difference between the observed and model data. The arrows mark indexed peaks. (For interpretation of the references to color in this figure legend, the reader is referred to the web version of this article.)

are partial extra framework Al species (as for MFS) and/or Brønsted sites interacting with non-exchanged potassium cations (see also below).

Upon interaction with CO, several previously well-described features [70] are observed in the spectra, and for brevity, we will focus mainly on the features which are particular for these catalysts. For SZR at low loadings, the Brønsted band (3613 cm^{-1}) is eroded and shifted to 3312 cm^{-1} as adducts between the Brønsted sites and the probe molecule are formed. This occurs before the erosion of the band at 3651 cm^{-1}, which appears to be linked to the appearance of the feature at 3483 cm^{-1}. Bands in this region have been linked to both a Fermi resonance phenomenon and the formation of adducts between hydroxyls on partial extra framework Al species and CO [70–72]. Given the apparent correspondence between the disappearance of the band at 3651 cm^{-1} and the appearance of the band at 3483 cm^{-1}, an assignment to partial extra framework Al becomes likely. Importantly, at higher loadings of CO, all strongly acidic hydroxyls are consumed by interaction with CO. In the CO stretching region, bands at 2172 and 2163 cm^{-1} appear at low loadings. The band at 2172 cm^{-1} can confidently be assigned to CO on Brønsted sites [70,72], whereas the band at 2163 cm^{-1} most likely is a composed of contributions from CO interacting with hydroxyls on partial extra framework Al species as well as CO interacting with potassium cations [73,74]. At higher loadings, a fraction of the silanols are consumed and the adducts between CO and silanols appear at 2158 cm^{-1}, overlapping with the band at 2163 cm^{-1} mentioned above. Physisorbed or liquid-like CO is seen at 2140 cm^{-1}. For MFS, the spectra are somewhat less complex. At low loadings of CO, the Brønsted band at 3613 cm^{-1} is shifted to 3287 cm^{-1}, and CO on Brønsted sites is evident at 2177 cm^{-1}. It may be noted that features associated with partial extra framework Al species are much less dominant and that no evidence of alkali cations are seen (no discernible band at

~2160 cm^{-1} and a much less pronounced feature at ~3470 cm^{-1} at low loadings). Upon increasing CO pressure, the silanol band is partially consumed, giving rise to absorption at 2157 cm^{-1}.

FT-IR spectra recorded during desorption of pyridine are shown in Fig. 4. Three main bands are expected and seen [57,75]. The band at 1541 cm^{-1} corresponds to CC stretching modes of protonated pyridine (Brønsted sites), whereas a band at 1453 cm^{-1} is expected for pyridine on Lewis acid sites. The band at 1490 cm^{-1} consists of overlapping contributions from both adsorption modes. Interestingly, for SZR, only a fraction of the Brønsted sites are accessible to pyridine (see inset). Moreover, it appears that the component at 3651 cm^{-1} is virtually unperturbed, even after the exposure to pyridine overnight. Fig. S.4 of the Supplementary Material shows the FT-IR spectra recorded during uptake of pyridine on SZR as a function of saturation time. In contrast, for MFS, all Brønsted sites were consumed after ~10 min exposure. No clear band corresponding to pyridine on Lewis acid sites is seen for SZR. Rather, a broad feature, which diminishes fairly rapid with increasing temperature, is seen in this spectral region. This is most likely related to pyridine interacting with potassium cations. Turning to the quantitative evaluation, a total acid site concentration of 0.49 mmol g^{-1}, which corresponds to an Si/Al ratio of 33, was found for MFS. This agrees well with the overall composition of the material and the value from TPD. The Brønsted/Lewis ratio was 15. For SZR, a Brønsted acid site concentration of 0.20 mmol g^{-1} was found, which is substantially less than inferred from composition as well as from TPD (see above). It was not possible to quantify the concentration of Lewis acid sites for SZR.

Fig. 5 displays TEM images (A and B) and the corresponding selected area electron diffraction (SAED) image (C) of an SZR crystal. The characteristic feature of the particles is the distinct needle shape. Typically, the needles are 2–5 μm long and 50–70 nm wide. Such a needle-like morphology was previously reported for the
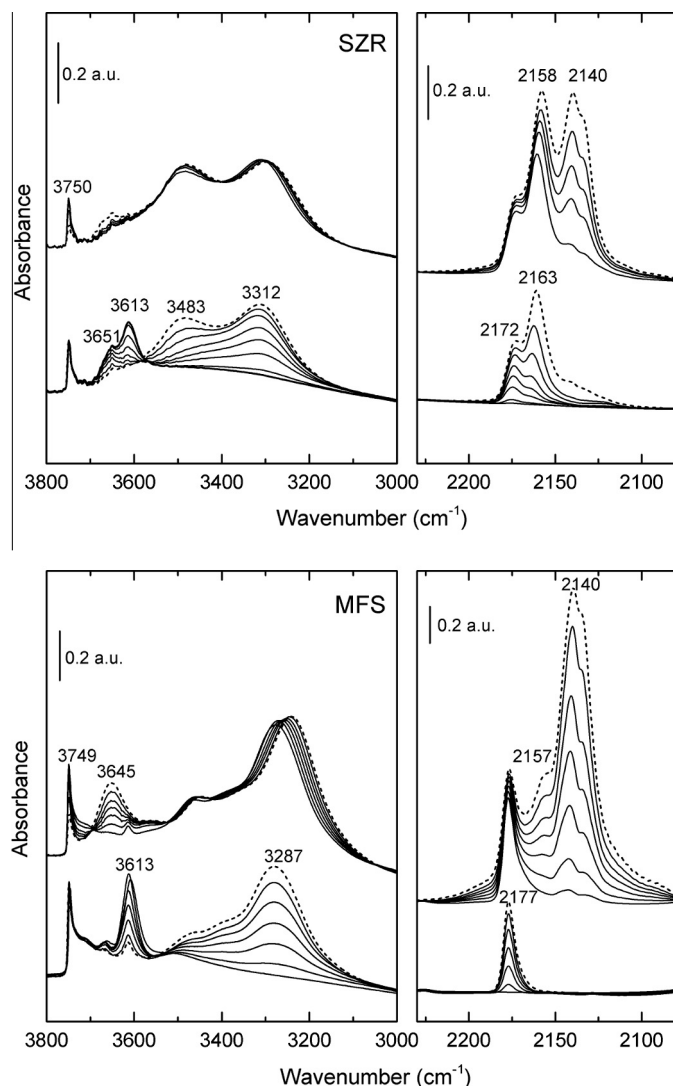
Fig. 3. FT-IR spectra for SZR (top panels) and MFS (bottom panels) upon interaction with CO. The left panels show the hydroxyl-stretching region and the right panels show the CO-stretching region. The bottom spectra in each panel correspond to low loading of CO (until near complete erosion of the Brønsted band) and the top spectra correspond to high loading.

material and appears to be favored [76]. Bragg spots in the direction of the needle were readily observed. Lattice spacings of ~7.46 Å, which corresponds to the c axis of the unit cell, were consistently observed. This confirms that the c direction of the unit cell runs in the direction of the needles. Once the c direction is correctly assigned, the orientation of the 8-ring and 10-ring channels is readily determined: the 10-ring channels are oriented along the c direction, that is, along the needles, and the 8-ring channels are perpendicular. This conclusion is supported by the bulk X-ray diffraction analysis (above) and crystal growth simulations (Fig. S.5 and Supplementary Material).

The same methods as described above for the SZR catalyst were employed to investigate MFS, see Fig. 6. The MFS crystals are pentagonal, but also highly defective and irregular. A platelet or nanosheet-type morphology is seen for this material. Typical sheets are 30–60 nm thick (B) with a longest distance of about 1.5 μm (A). Electron diffraction (D) revealed that the 10-ring channel system runs perpendicular to the sheets of MFS. Furthermore, the crystals are fivefold twinned (E, F), as also originally observed by Schlenker et al. [77]. It may be realized that the 8-ring channel

system would form a closed pentagon shape in defect free crystals, with no 8-rings exposed at the terminating crystal surfaces, that is a pore system exclusively connecting the interior surface of the crystals (F). In an actual, defective crystal, the access to the 8-rings is via the defect surfaces only. Thus, this catalyst may be described as an array of very short (30–60 nm) 10-ring pores exposed at both ends.

In order to provide a simple measure of the diffusion properties of some of the catalysts investigated, the uptake of the methanol reactant and that of a bulky inert hydrocarbon were investigated. As is evident from Fig. 7 (top panel), the uptake of 2,2-dimethylbutane is dramatically more pronounced for MFI and MFS compared with the other materials. The rate and the extent of the uptake appear to be comparable for these two materials, despite the one-dimensional nature of the MFS material. Further, the uptake is practically negligible for the other four catalysts. We do not attribute any significance to the marginally higher total uptake seen for SZR compared with CHA (for which no uptake is expected as the material has only 8-rings), FER, and TON. The main question to be answered is whether the large and fast uptake seen for MFS may be attributed to the short diffusion pathways (the 10-rings are 30–60 nm long only) or to the relatively large 10-rings (5.1 × 5.4 Å) compared with FER (4.2 × 5.4 Å), TON (4.6 × 5.7 Å), and SZR (4.1 × 5.2 Å). Unfortunately, data could not be recorded for *MRE (5.3 × 5.6 Å), which has relatively large 10-ring channels. However, in a similar and more extensive study, Wu et al. [78] investigated the uptake of several hydrocarbons in a range of zeolites. It was seen that *MRE behaved very similarly to TON (4.6 × 5.7 Å). Thus, it does not seem likely that the favorable uptake behavior seen here for MFS is related primarily to the comparatively large 10-rings in this material. Rather, the significantly faster and higher total uptake seen for the MFS catalyst compared with the other one-dimensional 10-ring materials may reasonably be attributed to the fast diffusion associated with the very short length of the 10-ring channels.

Turning to methanol (Fig. 7, bottom panel), a significant uptake of methanol is seen for all of the catalysts investigated. A plateau is reached within ~10 min for MFS, SZR, and TON, whereas a stable sample mass is reached after ~17 min for FER. For CHA, a slight increase in sample mass is seen after the initial large and rapid weight change. The final weights do not scale with BET surface area or acid site densities in a straightforward manner. Presumably, subtle differences in the free energy of adsorption among the frameworks, which would influence the adsorption equilibrium in an exponential term, will dominate. Nevertheless, it is evident that the methanol molecule, in contrast to 2,2-dimethylbutane, has easy and ample access to the internal surface of all these catalysts.

4.3. Catalyst performance

Fig. 8 shows the catalyst lifetime and product distribution for the MTH reaction over the different catalysts at 400 °C and WHSV = 2 gg⁻¹ h⁻¹. With respect to catalyst lifetime, it is clear from Fig. 1 that MFI vastly outperforms the other zeolites. The unique longevity of MFI is well documented and, along with selectivity toward high octane number gasoline components, forms the basis for the MTG process [11,12]. In contrast, SZR and FER deactivate extremely rapidly (the curves overlap). This is almost certainly due to the high acid site density and diffusion limitations imposed by the fairly large particles of the investigated materials (see also Supplementary Material for more details on the catalytic performance of SZR). For SZR, the significant content of partial extra framework Al might also contribute to deactivation. For CHA, a high density of only moderately strong acid sites in cages connected in three dimensions by small 8-ring windows leads to
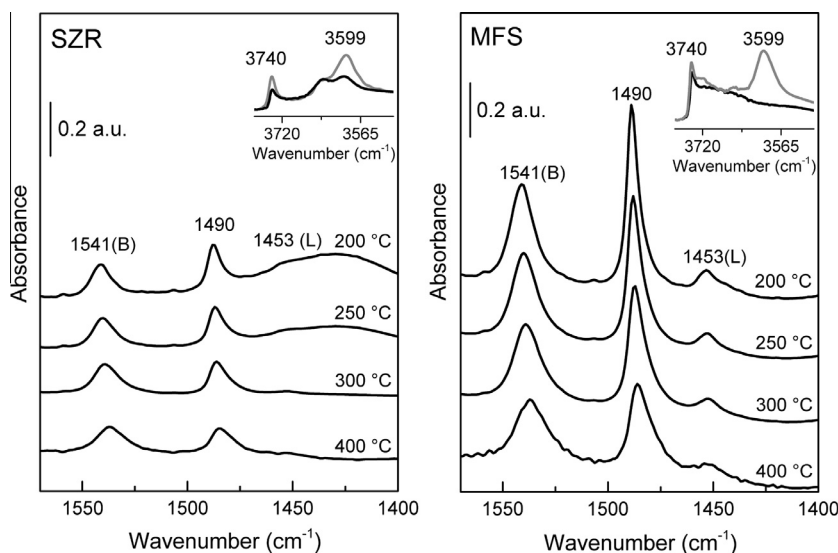
Fig. 4. FT-IR spectra for SZR (left panel) and MFS (right panel) upon desorption of pyridine. The spectra are reported after subtracting the spectrum of the activated zeolite. The insets show the hydroxyl stretching region (without subtraction) at 200 °C.
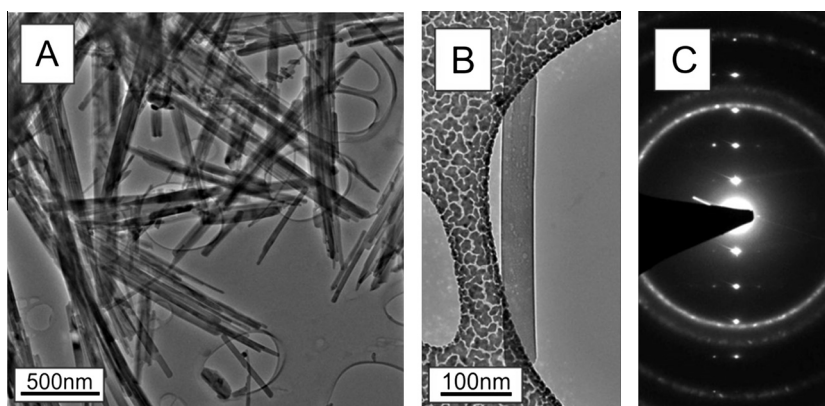

Fig. 5. Morphology analysis of SZR. (A) TEM image showing the general needle morphology. (B) TEM image of a needle lying on a holy carbon film coated with gold, which serves as an internal diffraction standard. (C) Selected area diffraction image of the area shown in (B). Powder rings are from the gold diffraction standard. The line of Bragg spots parallel to the needle morphology corresponds to a periodicity of 7.46 Å, which is the direction of the 10-ring channel system in SZR.

a moderate catalyst lifetime, giving rise to fluid bed operation in the MTO process [11,12]. The strictly unidirectional, medium-pore TON, MTT, EUO, and *MRE catalysts display lifetimes similar to that of CHA. It is generally accepted that zeolite catalysts with one- or two-dimensional pore systems suffer from more rapid deactivation than materials with three-dimensional porosity [79]. In contrast, for MFS, which does not have a three-dimensional pore system, an unexpectedly long lifetime is found. The origins of this feature will be discussed below.

Over the MFI, EUO, *MRE, MFS, TON, MTT, and FER catalysts, the majority of the product formed is C_{4+} hydrocarbons. This is as expected from medium-pore (10-ring) zeolites and in agreement with previous reports over such materials [11,13,51]. Notably, medium-pore zeolites TON, MTT, and FER yield a product rich in C_{5+}, which is very nearly free from aromatics, also in agreement with previous reports [13,51,80]. Medium-pore zeolites MFS, EUO, and *MRE convert methanol into a hydrocarbon mixture rich in aromatics; similar to that found for MFI, despite not having three-dimensional pore systems of intersecting 10-rings. For EUO, aromatics formation has been linked to side pockets on the external surface [13]. For MFS and *MRE on the other hand, aromatics formation must be due to the product shape selectivity

induced by the fairly large one-dimensional 10-rings, which are distinctly larger than those found in TON, MTT, and FER (Table 1). Small-pore (8-ring) CHA yields a product stream rich in light alkenes; the combined selectivity toward $C_2 + C_3$ hydrocarbons is 72%, which is also expected for the MTO catalyst. 10- and 8-ring zeolite SZR unexpectedly shows high selectivity toward the light hydrocarbons, C_2 and C_3 constitute 62%. In fact, the product spectrum observed for the medium-pore zeolite SZR is remarkably similar to the typical MTO product spectrum seen for small pore CHA, for which the 8-ring windows control the diffusion of molecules. The catalytic test results thus suggest that the selectivity of SZR also is controlled by the smaller 8-ring windows, despite the presence of 10-ring channels in the framework.

It is of some interest to investigate the C_{4+} fraction formed over some of the catalysts more closely. Fig. 9 shows that for CHA, this product fraction (which is undesired from an MTO perspective) is composed almost exclusively of the three linear butene isomers and some linear C_5 products. For SZR, on the other hand, a significantly larger amount of C_5 and even some C_6 compounds are seen. Looking at the distribution of the four butene isomers in detail, it is observed that MFI and TON yield a branched to linear ratio of 0.42 and 0.46, respectively, which is close to the equilibrium value.
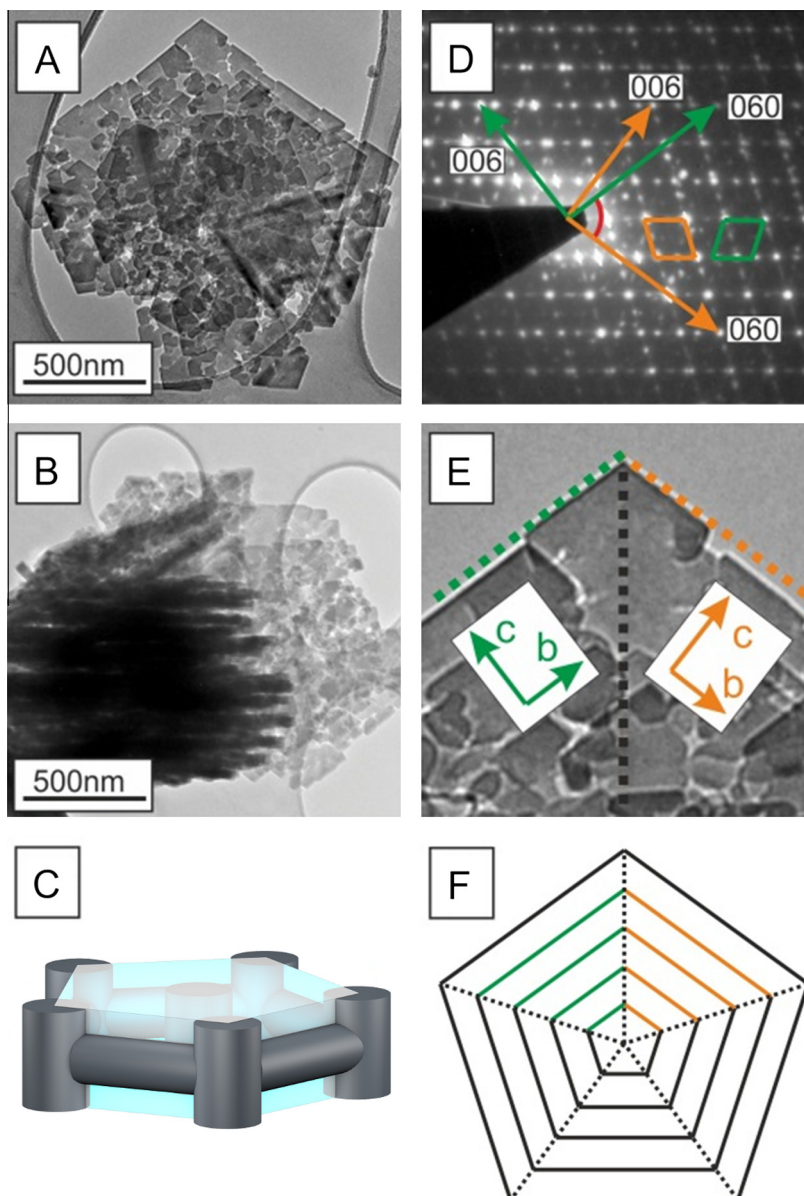
Fig. 6. Morphology analysis of MFS. Representative TEM images of plate shaped crystallites as viewed lying flat on the holy carbon film (A) and a stack of plates viewed edge on (B). (C) Schematic drawing of how the pore system could be embedded in the pentagonal plate morphology. (D) Selected area electron diffraction image of the area shown in (E). Twinning is clearly observed in (D) and the mapped twin boundary is shown in (E). (F) Schematic drawing of the twin boundaries (dotted lines) in a defect free crystallite. Orange and green colors correspond to the twin domains shown in (D) and (E). Full lines show how the 8-ring channel system forms a closed system with no termination at external surfaces. (For interpretation of the references to color in this figure legend, the reader is referred to the web version of this article.)

CHA, on the other hand, yields a ratio of only 0.05, as expected for a catalyst comprising only 8-rings. Finally, the SZR catalyst yields a ratio of 0.28, clearly lower than the equilibrium value.

5. Discussion

A major finding in this work is the remarkably high selectivity toward C_2 and C_3 products found for the 8- and 10-ring SZR catalyst, which is comparable to that typically observed for strictly 8-ring catalysts such as CHA. This observation was unexpected, as it was a priori reasonable to assume that the diffusion of product molecules would be enhanced through the 10-rings, thereby overshadowing the contribution of the 8-rings. Alternatively, one might expect the shape selectivity to be a mean of that typically observed for medium- and small-pore zeolites [81]. To shed light on this surprising behavior, it is important to know how the topology of the SZR material is embedded into the crystal morphology. The TEM and diffraction analysis (Fig. 5) clearly show that for SZR, the only access to the 10-rings is via the ends of the needles, whereas the external sides of the needles are covered by 8-ring pores. Considering a perfect cylinder with an aspect ratio (length/diameter) of 50 (representing a crystal of 2.5 μm length by 50 nm diameter), the ratio of the surface defined by the side of the cylinder to the surface defined by the bases is 100. This simple geometric argument leads to the conclusion that the shape selectivity of SZR is induced by the crystal morphology. This notion is visualized with the scheme presented in Fig. 10. A more detailed analysis of the product distribution sheds further light on the shape selectivity of this catalyst (Fig. 9). The non-negligible formation of C_{5+} products may reasonably be interpreted as products emerging from the 10-rings capping the needle-like crystals. However, when analyzing the
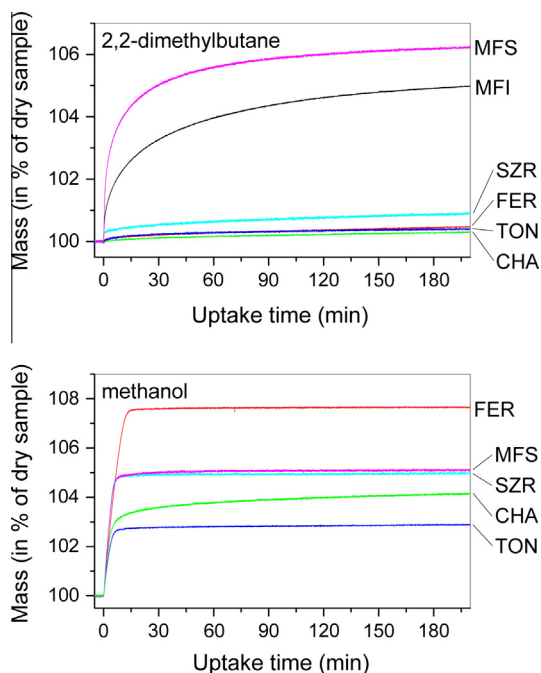
Fig. 7. Uptake of 2,2,-dimethylbutane (top panel) and methanol (bottom panel) at 100 °C on several zeolite catalysts.

distribution of the C₄ isomers, a notable preference for linear C₄ isomers is evident for SZR. This again indicates that the 8-ring pore openings, rather than the less abundant 10-rings, play a decisive role in determining the product shape selectivity for this catalyst.

The characterization data presented for SZR may also be rationalized according to the scheme in Fig. 10. A high surface area was found using nitrogen adsorption, uptake measurements show that methanol has easy access to a large internal surface/volume, and CO is able to interact with all strongly acidic sites distributed within the material. Clearly, these small probe molecules experience easy access the internal structure via both the 8- and 10-rings. However, when using larger probe molecules, virtually no access is seen for 2,2-dimethylbutane and a strongly restricted access is seen for pyridine, as the only possibility for these compounds to enter the internal volume is via the very scarce 10-rings.

The notion of selectivity engineering by preferential exposure of crystal facets that allow access to the particle interior via one set of pore openings, but not another, is conceptually different from most of the perspectives discussed in the introduction, which are based primarily on the shortening and lengthening of diffusion pathways. It is our opinion that these finding for SZR could open up for a new strategy to achieve selectivity control in zeolite catalysis. It is now straightforward to suggest that the concept of morphology-induced shape selectivity as introduced here may be explored further and extended to different framework topologies. However, for this approach to be applicable, the catalyst must comprise pore systems of distinct sizes. An obvious, but exceedingly demanding extension of this work would be to synthesize a series of, for example, SZR catalysts of differing aspect ratios and morphologies and to evaluate the resulting product distributions. Many other zeolite topologies would also be suited for such explorations. Clearly, this discussion is not independent of previous literature; the potential for selectivity control by using zeolite catalysts having channels of different diameter has been emphasized by Corma and co-workers [31,81,82] and links back to the idea of molecular traffic control originally introduced by Derouane [4].
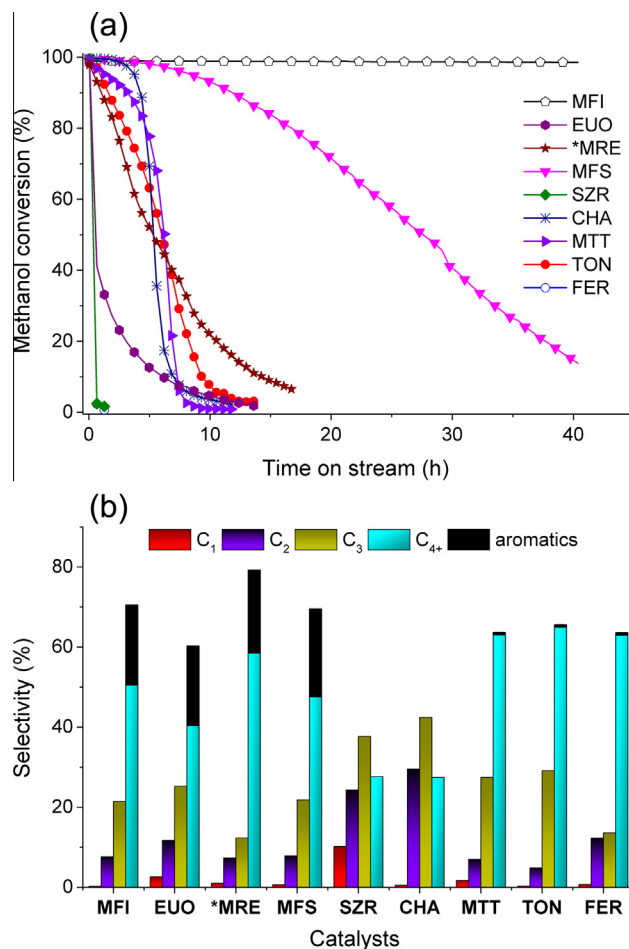

Fig. 8. Catalyst performance for nine different zeolite catalysts in the methanol to hydrocarbons reaction. (A) Methanol conversion versus time on stream at 400 °C and WHSV = 2 gg⁻¹ h⁻¹ and (B) product distribution at full conversion. The black-shaded area in the C₄₊ fraction corresponds to the amount of aromatics in the effluent.

It should be pointed out that both FER and MFS, which also have pore systems comprising both 10- and 8-rings, do not display this unusual product shape selectivity. However, for both FER and MFS, this is readily rationalized by analyzing the relation between pore systems and morphology. FER prefers a platelet morphology, for which the 8- and 10-ring channel openings are available on the edges of the platelets only, and the large flat facets are dense [63] (see also Supplementary Material). For MFS, the situation is similar, as the abundance of exposed 8-ring pore openings for this particular sample and morphology (see below) is limited. Thus, both FER and MFS as studied here do not offer a sufficient excess of 8-ring pore openings to facilitate morphology-induced shape selectivity. Moreover, by employing the line of reasoning outlined above, it is also possible to explain why in a rather gratifying manner.

It was shown above that MFS is fairly resistant toward deactivation. It is well known that lifetime is associated with the dimensionality of the catalyst pore system [79] and acid site density [83]. Nevertheless, MFS clearly outperforms the structurally related catalysts comprising one-dimensional 10-rings with similar acid site density. However, particle size, or more precisely diffusion lengths may also have a profound impact. Large crystal catalysts typically deactivate faster than catalysts comprising smaller (sub-micron or nanosized) crystals [53], and hierarchical mesoporous zeolites are often found to be more stable than regular, strictly microporous materials [84]. It was shown above (Fig. 6)
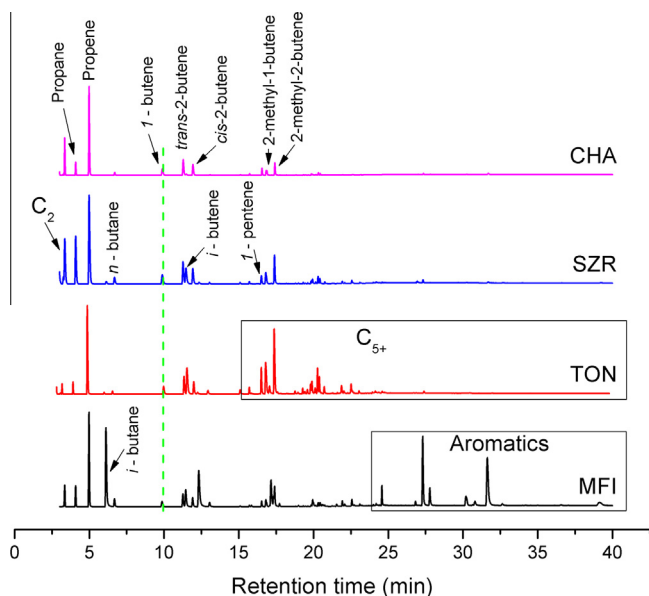
Fig. 9. GC–MS chromatograms of the product effluent from CHA (SAPO-34), SZR (SUZ-4), TON (ZSM-22), and MFI (ZSM-5) tested under identical reaction conditions after 5 min on stream (400 °C and WHSV = 2.05 gg^{-1} h^{-1}). C_1 is not included in the chromatograms.
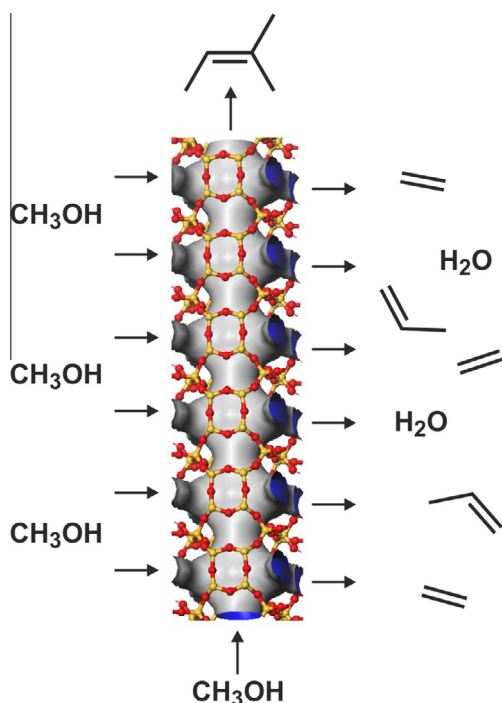

Fig. 10. Schematic illustrating the proposed morphology-controlled mechanism causing the unexpectedly high product selectivity toward the light C_1–C_3 fraction. The reactant (methanol) may enter the needles via both the ends and the sides. Heavier C_{5+} products and isobutene/isobutane can only escape via the ends of the needles, whereas the lighter products in addition will diffuse out of the abundant 8-ring openings that cover the sides of the needles.

that the MFS catalyst employed here displays a nanosheet-type morphology, where the length of the 10-ring channels is determined by the sheet thickness (30–60 nm). This in turn leads to favorable diffusion properties, as shown by uptake measurements (Fig. 7) and pyridine adsorption (Fig. 4). This constitutes a very plausible explanation for why the lifetime of the MFS catalyst is

markedly better than that seen for the structurally related EUO, *MRE, TON, and MTT catalysts, for which the 10-rings are several microns in length. Obviously, this is strongly related to the recent progress of Ryoo and co-workers [41,42] on the preparation of deactivation resistant ZSM-5 nanosheets, and, in general, work on layered zeolite-based materials [39,40].

6. Conclusions

Herein, the catalytic performance of nine different zeolite or zeotype catalysts has been investigated and compared in the conversion of methanol to hydrocarbons (MTH). Two of these topologies (SZR – SUZ-4 and MFS – ZSM-57) have not been employed as MTH catalysts previously. SZR yields a product spectrum rich in light alkenes (C_2 and C_3), but suffers from rapid deactivation, most likely due to being a diffusion restricted system and a high density of acid sites. Both will lead to coke accumulation. MFS yields a hydrocarbon product which is similar to the typical MFI MTG product, that is, an aromatics-rich mixture. The lifetime of MFS is longer than several structurally comparable catalysts, but still significantly shorter than for MFI.

For the SZR and MFS catalysts, the effect of morphology on catalyst performance is clearly observed. For MFS, the resistance toward deactivation appears to be due to a preferred platelet morphology, which results in short channels and therefore facile diffusion. SZR crystallizes preferably with needle-like morphology, and the 8- and 10-ring channels are accessed from the side and the end of the needle crystals, respectively. Consequently, the 8-ring channels unexpectedly dominate and control the product distribution during the MTH reaction, leading to *morphology-induced shape selectivity in zeolite catalysis*.

Finally, it should be pointed out that for both SZR and MFS, an analysis of how the framework topology is embedded into the actual crystals was instrumental to provide a rationalization of the observation made. Both materials comprise a combination of 8- and 10-ring channels, but for SZR, the 8-rings dominate. For MFS, on the other, the 8-rings are, in the extreme case of defect free crystals, not accessible from the crystal exterior at all.

Acknowledgments

Appendix A. Supplementary material

Supplementary data associated with this article can be found, in the online version, at http://dx.doi.org/10.1016/j.jcat.2015.03.013.

References

[1] S.M. Csicsery, Pure Appl. Chem. 58 (1986) 841.
[2] T.F. Degnan, J. Catal. 216 (2003) 32.
[3] S. Svelle, M. Bjørgen, in: A. Zecchina, S. Bordiga, E. Groppo (Eds.), Selective Nanocatalysts and Nanoscience: Concepts for Heterogeneous and Homogeneous Catalysis, Wiley-VCH Verlag GmbH & Co. KGaA, Weinheim, Germany, 2011, p. 237.
[4] E.G. Derouane, Z. Gabelica, J. Catal. 65 (1980) 486.
[5] D.S. Santilli, T.V. Harris, S.I. Zones, Microporous Mater. 1 (1993) 329.
[6] S. Lawton, M.E. Leonowicz, R. Partridge, P. Chu, M.K. Rubin, Microporous Mesoporous Mater. 23 (1998) 109.
[7] R. Parton, L. Uytterhoeven, J.A. Martens, P.A. Jacobs, G.F. Froment, Appl. Catal. 76 (1991) 131.

[8] W. Souverijns, J.A. Martens, G.F. Froment, P.A. Jacobs, J. Catal. 174 (1998) 177.
[9] J.A. Martens, W. Souverijns, W. Verrelst, R. Parton, G.F. Froment, P.A. Jacobs, Angew. Chem., Int. Ed. 34 (1995) 2528.
[10] M.C. Claude, J.A. Martens, J. Catal. 190 (2000) 39.
[11] U. Olsbye, S. Svelle, M. Bjørgen, P. Beato, T.V.W. Janssens, F. Joensen, S. Bordiga, K.P. Lillerud, Angew. Chem., Int. Ed. 51 (2012) 5810.
[12] M. Stöcker, Microporous Mesoporous Mater. 29 (1999) 3.
[13] S. Teketel, W. Skistad, S. Benard, U. Olsbye, K.P. Lillerud, P. Beato, S. Svelle, ACS Catal. 2 (2012) 26.
[14] R. Ravishankar, D. Bhattacharya, N.E. Jacob, S. Sivasanker, Microporous Mater. 4 (1995) 83.
[15] C. Baerlocher, L.B. McCusker, Database of Zeolite Structures. <http://www.iza-structure.org/databases/>.
[16] B. Smit, T.L.M. Maesen, Nature 451 (2008) 671.
[17] B. Smit, T.L.M. Maesen, Chem. Rev. 108 (2008) 4125.
[18] G.J. Hutchings, C.J. Kiely, Acc. Chem. Res. 46 (2013) 1759.
[19] P.L. Hansen, J.B. Wagner, S. Helveg, J.R. Rostrup-Nielsen, B.S. Clausen, H. Topsøe, Science 295 (2002) 2053.
[20] G. Ertl, Angew. Chem., Int. Ed. 47 (2008) 3524.
[21] T.O. Drews, M. Tsapatsis, Curr. Opin. Colloid Interface Sci. 10 (2005) 233.
[22] K. Li, J. Valla, J. Garcia-Martinez, ChemCatChem 6 (2014) 46.
[23] R. Chal, C. Gerardin, M. Bulut, S. van Donk, ChemCatChem 3 (2011) 67.
[24] K. Egeblad, C.H. Christensen, M. Kustova, C.H. Christensen, Chem. Mater. 20 (2008) 946.
[25] K. Möller, T. Bein, Chem. Soc. Rev. 42 (2013) 3689.
[26] J. Perez-Ramirez, C.H. Christensen, K. Egeblad, C.H. Christensen, J.C. Groen, Chem. Soc. Rev. 37 (2008) 2530.
[27] D.P. Serrano, J.M. Escola, P. Pizarro, Chem. Soc. Rev. 42 (2013) 4004.
[28] S. van Donk, A.H. Janssen, J.H. Bitter, K.P. de Jong, Catal. Rev. 45 (2003) 297.
[29] S. Al-Khattaf, S.A. Ali, A.M. Aitani, N. Zilkova, D. Kubicka, J. Cejka, Catal. Rev.: Sci. Eng. 56 (2014) 333.
[30] D. Verboekend, J. Perez-Ramirez, Catal. Sci. Technol. 1 (2011) 879.
[31] A. Corma, J. Catal. 216 (2003) 298.
[32] J. Jiang, J. Yu, A. Corma, Angew. Chem., Int. Ed. 49 (2010) 3120.
[33] L. Tosheva, V.P. Valtchev, Chem. Mater. 17 (2005) 2494.
[34] T. Alvaro-Munoz, E. Sastre, C. Marquez-Alvarez, Catal. Sci. Technol. 4 (2014) 4330.
[35] R. Khare, D. Millar, A. Bhan, J. Catal. 321 (2015) 23.
[36] C.-J. Jia, Y. Liu, W. Schmidt, A.-H. Lu, F. Schüth, J. Catal. 269 (2010) 71.
[37] R.A. Schoonheydt, Angew. Chem., Int. Ed. 47 (2008) 9188.
[38] L. Karwacki, M.H.F. Kox, D.A.M. deWinter, M.R. Drury, J.D. Meeldijk, E. Stavitski, W. Schmidt, M. Mertens, P. Cubillas, N. John, A. Chan, N. Kahn, S.R. Bare, M. Anderson, J. Kornatowski, B.M. Weckhuysen, Nat. Mater. 8 (2009) 959.
[39] U. Diaz, A. Corma, Dalton Trans. 43 (2014) 10292.
[40] W.J. Roth, P. Nachtigall, R.E. Morris, J. Cejka, Chem. Rev. 114 (2014) 4807.
[41] M. Choi, K. Na, J. Kim, Y. Sakamoto, O. Terasaki, R. Ryoo, Nature 461 (2009) 246.
[42] J. Kim, M. Choi, R. Ryoo, J. Catal. 269 (2010) 219.
[43] S. Jiang, Y.K. Hwang, S.H. Jhung, J.S. Chang, J.S. Hwang, T.X. Cai, S.E. Park, Chem. Lett. 33 (2004) 1048.
[44] F. Bleken, W. Skistad, K. Barbera, M. Kustova, S. Bordiga, P. Beato, K.P. Lillerud, S. Svelle, U. Olsbye, Phys. Chem. Chem. Phys. 13 (2011) 2539.
[45] M. Guisnet, J.-P. Gilson, in: M. Guisnet, J.-P. Gilson (Eds.), Zeolites for Cleaner Technology, Catalysis Science Series, vol. 3, Imperial College Press, London, 2002, p. 1.
[46] W. Vermeiren, J.-P. Gilson, Top. Catal. 52 (2009) 1131.
[47] J.B. Nagy, J.P. Gilson, E.G. Derouane, J. Mol. Catal. 5 (1979) 393.
[48] S. Mintova, J.-P. Gilson, V. Valtchev, Nanoscale 5 (2013) 6693.
[49] F.C. Meunier, D. Verboekend, J.-P. Gilson, J.C. Groen, J. Perez-Ramirez, Microporous Mesoporous Mater. 148 (2012) 115.
[50] X. Chen, T. Todorova, A. Vimont, V. Ruaux, Z. Qin, J.-P. Gilson, V. Valtchev, Microporous Mesoporous Mater. 200 (2014) 334.
[51] S. Teketel, S. Svelle, K.P. Lillerud, U. Olsbye, ChemCatChem 1 (2009) 78.
[52] S.H. Lee, C.H. Shin, G.J. Choi, T.J. Park, I.S. Nam, B. Han, S.B. Hong, Microporous Mesoporous Mater. 60 (2003) 237.
[53] B.P.C. Hereijgers, F. Bleken, M. Hellner Nilsen, S. Svelle, M. Bjørgen, K.P. Lillerud, B.M. Weckhuysen, U. Olsbye, J. Catal. 264 (2009) 77.
[54] A. Katerinopoulou, T. Balic-Zunic, L.F. Lundegaard, J. Appl. Crystallogr. 45 (2012) 22.
[55] R.J. Gorte, Catal. Lett. 62 (1999) 1.
[56] C. Pereira, R.J. Gorte, Appl. Catal. A 90 (1992) 145.
[57] E. Selli, L. Forni, Microporous Mesoporous Mater. 31 (1999) 129.
[58] A. Zecchina, G. Spoto, S. Bordiga, Phys. Chem. Chem. Phys. 7 (2005) 1627.
[59] K. Chakarova, K. Hadjiivanov, J. Phys. Chem. C 115 (2011) 4806.
[60] J. Sauer, K.P. Schröder, V. Termath, Collect. Czech. Chem. Commun. 63 (1998) 1394.
[61] S. Bordiga, L. Regli, D. Cocina, C. Lamberti, M. Bjørgen, K.P. Lillerud, J. Phys. Chem. B 109 (2005) 2779.
[62] R. Shah, J.D. Gale, M.C. Payne, Chem. Commun. (1997) 131.
[63] A. Bonilla, D. Baudouin, J. Perez-Ramirez, J. Catal. 265 (2009) 170.
[64] M.A. Asensi, M.A. Camblor, A. Martinez, Microporous Mesoporous Mater. 28 (1999) 427.
[65] S. Gao, X. Wang, X. Wang, Y. Bai, Microporous Mesoporous Mater. 174 (2013) 108.
[66] P. Worathanakul, D. Trisuwan, A. Phatruk, P. Kongkachuichay, Colloids Surf., A 377 (2011) 187.
[67] B. Louis, S. Walspurger, J. Sommer, Catal. Lett. 93 (2004) 81.
[68] S.L. Lawton, J.M. Bennett, J.L. Schlenker, M.K. Rubin, J. Chem. Soc., Chem. Commun. (1993) 894.
[69] V.L. Zholobenko, D.M. Lukyanov, J. Dwyer, W.J. Smith, J. Phys. Chem. B 102 (1998) 2715.
[70] A. Zecchina, S. Bordiga, G. Spoto, D. Scarano, G. Petrini, G. Leofanti, M. Padovan, C. Otero Arean, J. Chem. Soc. Faraday Trans. 88 (1992) 2959.
[71] K. Chakarova, K. Hadjiivanov, Chem. Commun. 47 (2011) 1878.
[72] S. Bordiga, E. Escalona Platero, C. Otero Arean, C. Lamberti, A. Zecchina, J. Catal. 137 (1992) 179.
[73] S. Bordiga, G. Turnes Palomino, C. Paze, A. Zecchina, Microporous Mesoporous Mater. 34 (2000) 67.
[74] R. Bulanek, E. Koudelkova, Microporous Mesoporous Mater. 151 (2012) 149.
[75] C.A. Emeis, J. Catal. 141 (1993) 347.
[76] W. Zhang, Y. Wu, J. Gu, H. Zhou, J. Wang, Mater. Res. Bull. 46 (2011) 1451.
[77] J.L. Schlenker, J.B. Higgins, E.W. Valyocsik, Zeolites 10 (1990) 293.
[78] E.L. Wu, G.R. Landolt, A.W. Chester, Stud. Surf. Sci. Catal. 28 (1986) 547.
[79] M. Guisnet, L. Costa, F.R. Ribeiroa, J. Mol. Catal. A 305 (2009) 69.
[80] J.F. Haw, W. Song, D.M. Marcus, J.B. Nicholas, Acc. Chem. Res. 36 (2003) 317.
[81] A. Corma, Microporous Mesoporous Mater. 21 (1998) 487.
[82] R. Simancas, D. Dari, N. Velamazan, M.T. Navarro, A. Cantin, J.L. Jorda, G. Sastre, A. Corma, F. Rey, Science 330 (2010) 1219.
[83] M. Bjørgen, S. Kolboe, Appl. Catal. A 225 (2002) 285.
[84] M. Bjørgen, F. Joensen, M. Spangsberg Holm, U. Olsbye, K.P. Lillerud, S. Svelle, Appl. Catal. A 345 (2008) 43.